Measurements of Cylindrical Ice Crystal Growth Limited by Combined Particle and Heat Diffusion

Kenneth G. Libbrecht

Department of Physics, California Institute of Technology
Pasadena, California 91125

Abstract. We present measurements of the growth of long columnar ice crystals from water vapor over a broad range of temperatures and supersaturation levels in air. Starting with thin, c-axis ice needle crystals, we observed their subsequent growth behavior in a vapor diffusion chamber, extracting the initial radial growth velocities of the needles under controlled conditions. Approximating the hexagonal needle crystals as infinitely long cylinders, we created an analytical growth model that includes effects from particle diffusion of water molecules through the surrounding air along with the diffusion of heat generated by solidification. With only minimal adjustment of model parameters, we obtained excellent agreement with our experimental data. To our knowledge, this is the first time that the combined effects from particle and heat diffusion have been measured in ice growth from water vapor. This analysis further provides an accurate method for calibration of the water-vapor supersaturation levels in experimental growth chambers.

1 Introduction

We recently developed a novel dual diffusion chamber for observing the growth of ice crystals from water vapor in air, which allows us to create slender needle crystals and measure their subsequent growth behavior under carefully controlled conditions. The experimental apparatus is described in some detail in [1]. Figure 1 shows an example of a thin, plate-like ice crystal growing on the end of a long ice needle at a temperature of -15 C. Our overarching goal with these observations is to develop a comprehensive model of ice crystal growth from water vapor that can reproduce quantitative growth rates as well as growth morphologies over a broad range of circumstances. Although ice crystal formation has been studied extensively for many decades, our understanding of the physical effects governing growth behaviors at different temperatures and supersaturations is still rather poor [2, 3, 4, 5, 6, 7, 8].

Determining the water vapor supersaturation in ice growth experiments done in air has long been a challenge, and it remains a significance hindrance to making accurate, quantitative ice growth measurements. While a small thermistor probe can easily determine air temperatures with excellent absolute accuracy and little perturbation of the surrounding environment, water vapor probes (hygrometers) are typically bulky and quite limited in absolute accuracy. Moreover, in a supersaturated environment, water vapor condenses on solid surfaces, and the presence of unwanted ice surfaces can greatly affect the supersaturation field in their vicinity. As a result, one often resorts to modeling of the experimental chamber to determine the supersaturation within.

The second diffusion chamber in our dual-chamber apparatus was carefully designed to facilitate accurate modeling of the water vapor supersaturation [1]. The top and bottom surfaces have con-

stant, well controlled temperatures, and the side walls were constructed to maintain a simple, linear vertical temperature gradient throughout the chamber. All walls of the chamber are coated with ice crystals during operation, thus providing well-defined boundary conditions for constructing a heat and water vapor diffusion model of the interior of the chamber.

Figure 1: This photograph shows a typical c-axis ice needle crystal growing at -15 C. The supporting wire substrate is seen in the lower left of the photo, covered with a large number of frost crystals. Several thin, c-axis ice needles grew out from the wire tip, and one was brought into focus with the entire needle in the image plane. After 95 seconds of growth at a water-vapor supersaturation of $\sigma_{center} \approx 11$ percent (in this particular example) a thin ice plate can be seen growing on the tip of the ice needle, here seen in side view. The ice plate diameter, ice needle diameter below the plate, and the overall needle length can be extracted from a set of similar calibrated images.

1.1 Supersaturation in the Diffusion Chamber

The temperatures of the top and bottom of the second diffusion chamber were defined by $T_{top,bottom} = T_{set} \pm \Delta T$, so $T_{top} - T_{bottom} = 2\Delta T$ (see [1] for the chamber dimensions), and the temperatures of the four walls were maintained at $T_{walls}(z) = T_{bottom} + 2\Delta T(z - z_{bottom})/(z_{top} - z_{bottom})$. Solving the heat diffusion equation within the chamber then yields the air temperature $T_{air}(z) = T_{walls}(z)$, and in particular we have $T_{center} = (T_{top} + T_{bottom})/2$ at the center of the chamber. Moreover, the

temperature gradient inhibits convective air currents within the chamber. A shutter on one wall of the chamber is opened briefly to allow the transport of crystals into the chamber, but it is otherwise kept closed to maintain a stable temperature profile within the chamber.

If we first imagine moving the side walls of the chamber out to infinity, then we can use a plane-parallel approximation to estimate the water-vapor supersaturation at the chamber center, where test crystals are positioned. Solving the diffusion equation for water vapor density $c(z)$ yields a linear function with a constant gradient dc/dz and $c_{center} = (c_{top} + c_{bottom})/2$, yielding the supersaturation at the center of the chamber

$$\begin{aligned} \sigma_{center} &= \frac{c_{center} - c_{sat}(T_{center})}{c_{sat}(T_{center})} \\ &= \frac{1}{2}\frac{c_{sat}(T_{top}) - 2c_{sat}(T_{center}) + c_{sat}(T_{bottom})}{c_{sat}(T_{center})} \end{aligned} \tag{1}$$

where $c_{sat}(T)$ is the saturated vapor pressure above an ice surface. This expression gives the exact value for σ_{center} in the plane-parallel approximation (ignoring small changes in the diffusion constant with temperature).

For small ΔT, we expand the above expression to obtain the simpler expression

$$\begin{aligned} \sigma_{center} &\approx \frac{1}{2}\frac{1}{c_{sat}(T_{center})}\frac{d^2 c_{sat}}{dT^2}(T_{center})\,(\Delta T)^2 \\ &\approx C_{diff}(T_{center})\,(\Delta T)^2 \end{aligned} \tag{2}$$

The function $C_{diff}(T)$ can be calculated using $c_{sat}(T) \sim \exp(-6150/T_K)$ to good accuracy, where T_K is the temperature in Kelvin. In practice, we have found that the quadratic expansion is usually accurate enough for our purposes, as it differs from the exact expression for σ_{center} by less than a percent when $\Delta T < 6$ C, and it is only a few percent high when $\Delta T = 10$ C.

To see how the chamber walls and the crystal support structure affected the supersaturation field, we examined a range of computational models of the diffusion chamber under different conditions, with one example shown in Figure 2. In these models we solved the dual-diffusion problem (temperature and water-vapor density) numerically in three dimensions. We found that, over a broad range of conditions near $T_{center} \approx -15$ C, the side walls reduced σ_{center} by a factor of approximately 0.8 compared to the plane-parallel approximation, and an ice-covered central stem further reduced σ_{center} by a factor of approximately 0.9. Combined, our models indicated that these effects lowered the supersaturation at the center by a constant geometrical factor of $G_{mod} \approx 0.72$ compared with the plane-parallel approximation, so that Equation 2 becomes

$$\sigma_{center}(T_{center}, \Delta T) \approx G_{mod} C_{diff}(T_{center})\,(\Delta T)^2 \tag{3}$$

Our models also indicated, however, that there remained significant uncertainty in our ability to calculate G_{mod}, arising mostly from difficulties in accurately modeling effects from the crystal support structure and from a microscope objective placed inside the chamber about 90 mm away (horizontally) from the growing crystals.

1.2 Modeling Cylindrical Crystal Growth

As we began measuring crystal growth rates with this apparatus, we soon realized that the radial growth of the ice needles could be used to calibrate the supersaturation σ_{center} as a function of T_{center}

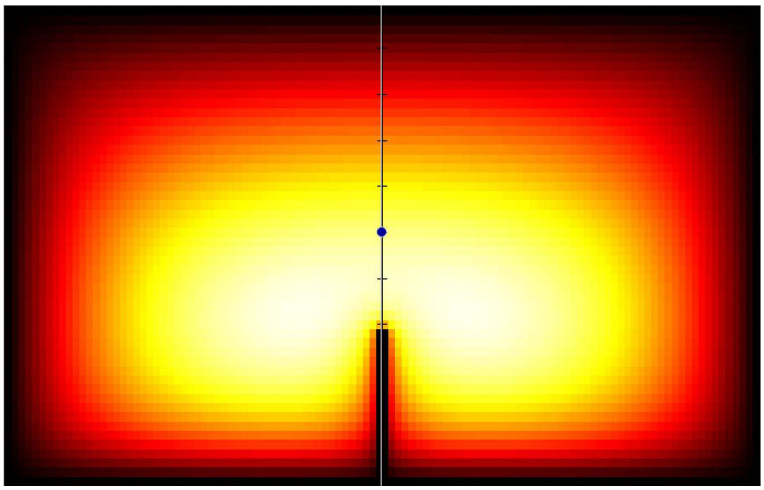

Figure 2: An example numerical model of the second diffusion chamber described in [1], showing a contour plot of the water vapor supersaturation within the chamber. The edges of the plot represent the outer walls of the chamber, and the observation point is at the geometrical center of the chamber, marked here with a round dot. Note that the supersaturation drops to zero at the chamber walls (dark), and reaches its maximum value (white) below the center of the chamber. In this particular model, the supersaturation also goes to zero near an ice-covered central post that supports the test crystals.

and ΔT. In essence, the prism surfaces of the columnar needles serve as "witness" surfaces, providing a fairly accurate measure of the surrounding water vapor supersaturation. As we will see below, this calibration works because the radial growth of the needles is limited primarily by particle and heat diffusion, and is nearly independent of the attachment coefficient α_{prism} at the needle surface. Therefore we do not need to know α_{prism} with great accuracy to calibrate $\sigma_{center}(T_{center}, \Delta T)$.

To see this, consider the growth of an infinitely long cylindrical ice crystal. Ignoring latent heat generation for the moment, we can solve the particle diffusion equation in cylindrical coordinates to yield the general solution $\sigma(r) = C_1 + C_2 \log(r)$, where C_1 and C_2 are constants to be determined by the boundary conditions in the equation. Here we have approximated the diffusion equation by Laplace's equation, which is quite accurate in this situation, as the dimensionless Peclet number is much less than unity [8].

At the outer boundary of this model we assume a constant supersaturation $\sigma(R_{far}) = \sigma_{far}$, where R_{far} is the outer boundary of the cylindrically symmetric diffusion field, and σ_{far} is essentially equal to σ_{center} described above. (Note that R_{far} cannot be set to infinity in cylindrical coordinates, as is commonly done in spherical coordinates.) Equating σ_{far} with σ_{center} ignores the particle density gradient dc/dz in the diffusion chamber, which is justified by the observation that vertical asymmetries in crystal growth rates are generally quite small.

At the inner boundary R_{in}, equal to the surface of the cylindrical crystal, we write the radial growth velocity

$$v = \frac{dR_{in}}{dt} = \frac{c_{sat} D}{c_{ice}} \frac{d\sigma}{dr}(R_{in}) = \alpha_{prism} v_{kin} \sigma(R_{in}) \tag{4}$$

where $D \approx 2 \times 10^{-5}$ m/sec^2 is the particle diffusion constant, c_{ice} is the number density of ice, and $v_{kin}(T)$ is the kinetic velocity defined in [8]. Including these boundary conditions in the solution for $\sigma(r)$ then gives

$$v = \frac{\alpha_{prism}\alpha_{diffcyl}}{\alpha_{prism} + \alpha_{diffcyl}} v_{kin}\sigma_{far} \tag{5}$$

where

$$\alpha_{diffcyl} = \frac{1}{B}\frac{X_0}{R_{in}}, \tag{6}$$

with $B = \log(R_{far}/R_{in})$ and $X_0 = c_{sat}D/c_{ice}v_{kin} \approx 0.145$ μm. This cylindrical solution is similar to the spherical case presented in [8].

Using typical numbers (as we will see below) of $R_{in} = 5$ μm and $R_{far} = 2$ cm, we obtain the rather small value

$$\alpha_{diffcyl} \approx 0.0035$$

Comparing this $\alpha_{diffcyl}$ with the α_{prism} measurements presented in [9], we find that $\alpha_{diffcyl} \ll \alpha_{prism}$ in most circumstances, allowing us to write

$$v \approx \alpha_{diffcyl} v_{kin}\sigma_{far} \tag{7}$$

and we see that this growth velocity is independent of α_{prism} as long as $\alpha_{diffcyl} \ll \alpha_{prism}$. Combining Equations 3, 6, and 7 then yields the radial growth rate of the cylinder

$$v(R_{in}) \approx \frac{G_{mod}}{B}\frac{X_0}{R_{in}} v_{kin} C_{diff}(T)\,(\Delta T)^2 \tag{8}$$

This equation gives us a good prediction for $v(R_{in})$, as all the parameters are rather tightly constrained except for G_{mod} (which is determined roughly by our modeling of the experimental chamber, as described above) and $B = \log(R_{far}/R_{in})$. However, Equation 8 only applies in the absence of crystal heating from solidification, which produces a significant perturbation of $v(R_{in})$, so we next examine thermal considerations in our cylindrical crystal model.

Heating occurs because the growth of the cylindrical crystal releases a latent heat per unit length of

$$\frac{dQ}{dLdt} = 2\pi\lambda\rho v R_{in}$$

where $\lambda = 2.8 \times 10^6$ J/kg is the latent heat for the vapor/solid transition and $\rho = 917$ kg/m^3 is the ice density. This generated heat must then be removed via conduction through the air surrounding the crystal (ignoring convective air currents). Solving the heat diffusion equation in cylindrical coordinates is similar to solving the particle diffusion equation described above, and doing so yields a temperature rise of the crystal (relative to the air temperature at $r = R_{far}$) given by

$$\delta T = \frac{B\lambda\rho v R_{in}}{\kappa} \tag{9}$$

where $\kappa = 0.025$ W m^{-1} K^{-1} is the thermal conductivity of air. The temperature rise increases the equilibrium vapor pressure of the ice to

$$c(R_{in}) \approx c_{sat}(T_{far})\,[1 + \eta\delta T]$$

where $\eta = d\log\left(c_{sat}\right)/dT$, and a bit of algebra reveals that this reduces the growth rate to (see [8])

$$v(R_{in}) \approx \frac{1}{1+\chi_0}\frac{G_{mod}}{B}\frac{X_0}{R_{in}}v_{kin}C_{diff}\left(\Delta T\right)^2 \tag{10}$$

where

$$\chi_0 = \frac{\eta D\lambda\rho}{\kappa}\frac{c_{sat}}{c_{ice}}$$

This result is an extension of Equation 8, and $v\left(R_{in}, T, \Delta T\right)$ in Equation 10 provides our final theoretical prediction for the growth rates of cylindrical crystals in our diffusion chamber. Our next step is to compare these predicted growth rates with experimental data.

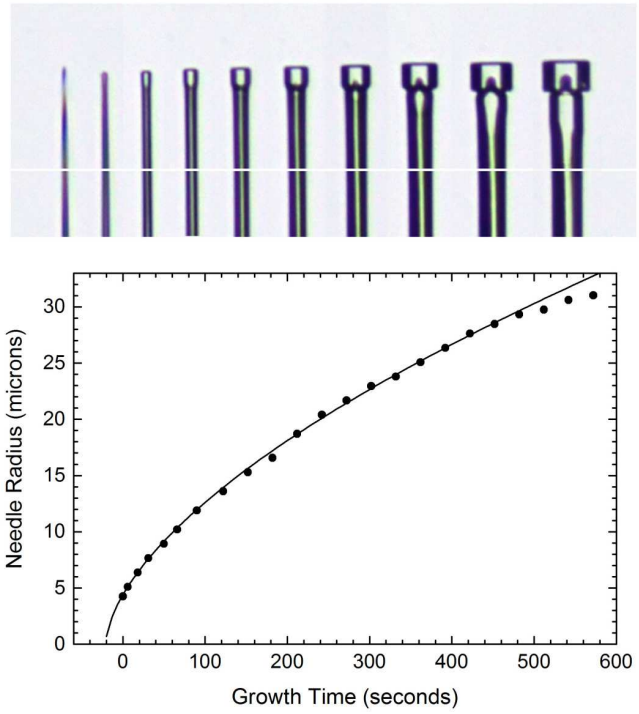

Figure 3: The top panel shows a composite image of the tip of a single ice needle crystal as it grew. The graph below it shows the needle radius at a location 100 μm below the needle tip, as indicated by the white horizontal line in the composite image. The images correspond to the first ten points in the graph. The needle grew in our diffusion chamber at a center temperature of $T_{center} = -2$ C with $\Delta T = 7$ C.

2 Comparison with Crystal Growth Measurements

For all the crystal growth data presented here, we first measured the needle radius as a function of time $R_{needle}(t)$, at a location $L = 100$ μm below the needle tip, starting from images similar to that shown in Figure 1. Figure 3 shows one example crystal grown at a temperature of $T = -2$ C and $\Delta T = (T_{top} - T_{bottom})/2 = 7$ C. This choice of L was something of a compromise, being close enough to the needle tip to be relevant for subsequent observations of ice structures at the tip, while far enough below the tip that these same structures did not greatly influence $R_{needle}(t)$ for small R_{needle}.

The optical microscope used to photograph the crystal had a resolving power of 2.5 μm, and the image pixels measured 0.85 μm. Our diameter resolution was therefore about ± 2 μm, giving radial measurements that were accurate to about ± 1 μm. We then fit the $R_{needle}(t)$ data to a smooth curve to determine $v = dR_{needle}/dt$ at a time when $R_{needle} = 5$ μm, as shown in Figure 3. We chose the smallest practical R_{needle} for which we could accurately measure dR_{needle}/dt, because the tip structures more greatly perturbed the cylinder growth at later times, when the tip structures (especially plates) were larger in size. We did observe some variation in the measured dR_{needle}/dt with changing L, with different tip structures, and between different crystals grown in ostensibly the same conditions. But these variations were at roughly the ± 20 percent level, so they did not alter our analysis greatly.

Figure 4 shows the resulting radial growth velocity $v_5(T, \Delta T) = v(R_{needle} = 5$ μm$)$ measured at two representative growth temperatures as a function of ΔT. These data, along with similar data at other temperatures, were well fit with simple quadratic functions $v_5(T, \Delta T) = A_5(T)\Delta T^2$. The measured fit coefficients $A_5(T)$ were then compared with calculated $A_5(T)$ from Equation 10, and the results are summarized in Figure 5. The theory curves used $G_{mod} = 0.72$, and R_{far} was adjusted to fit the particle+heat diffusion curve to the data, yielding a best fit $R_{far} = 2$ cm. As can be seen in Figure 5, our data are in excellent agreement with the expected particle+heat diffusion prediction over the entire temperature range tested, with a physically reasonable choice for R_{far}.

From this comparison between theory and experiment, we can extract a prediction for $\sigma_{far}(T, \Delta T)$, essentially equal to σ_{center}, the supersaturation at the center of the diffusion chamber in the absence of any test crystals. Parameterizing this as $\sigma_{far}(T, \Delta T) = A_\sigma(T)\Delta T^2$, the lower theory curve in Figure 5 becomes the $A_\sigma(T)$ curve shown in Figure 6. The calculated $\sigma_{far}(T, \Delta T) = A_\sigma(T)\Delta T^2$, using $R_{far} = 2$ cm extracted from the data, then replaces Equation 3 as our best estimate of the supersaturation at the center of our diffusion chamber, now calibrated using experimental data.

In summary, we have modeled the early growth of ice needle crystals in a vapor diffusion chamber using a cylindrically symmetric approach that approximates the needles as infinitely long cylinders. The largely analytical model (with the geometrical correction factor G_{mod} provided by numerical simulations) then yielded Equation 10, which gives the radial growth velocity $v(R_{in})$ as a function of T, ΔT, and other experimental parameters. Comparing this predicted $v(R_{in})$ with measurements at $R_{in} = 5$ μm, we found excellent agreement using a sensible value of $R_{far} = 2$ cm for the outer boundary in the model.

The data clearly indicate that both heat diffusion and particle diffusion limit the crystal growth rates, as theory predicts. To our knowledge, this is the first time that ice growth experiments have achieved sufficient absolute accuracy to verify this basic theoretical prediction. Having a reliable understanding of the supersaturation and resulting crystal growth behavior for this simple cylindrical geometry is a major step forward in producing accurate, quantitative measurements and models of more complex ice crystal growth behaviors.

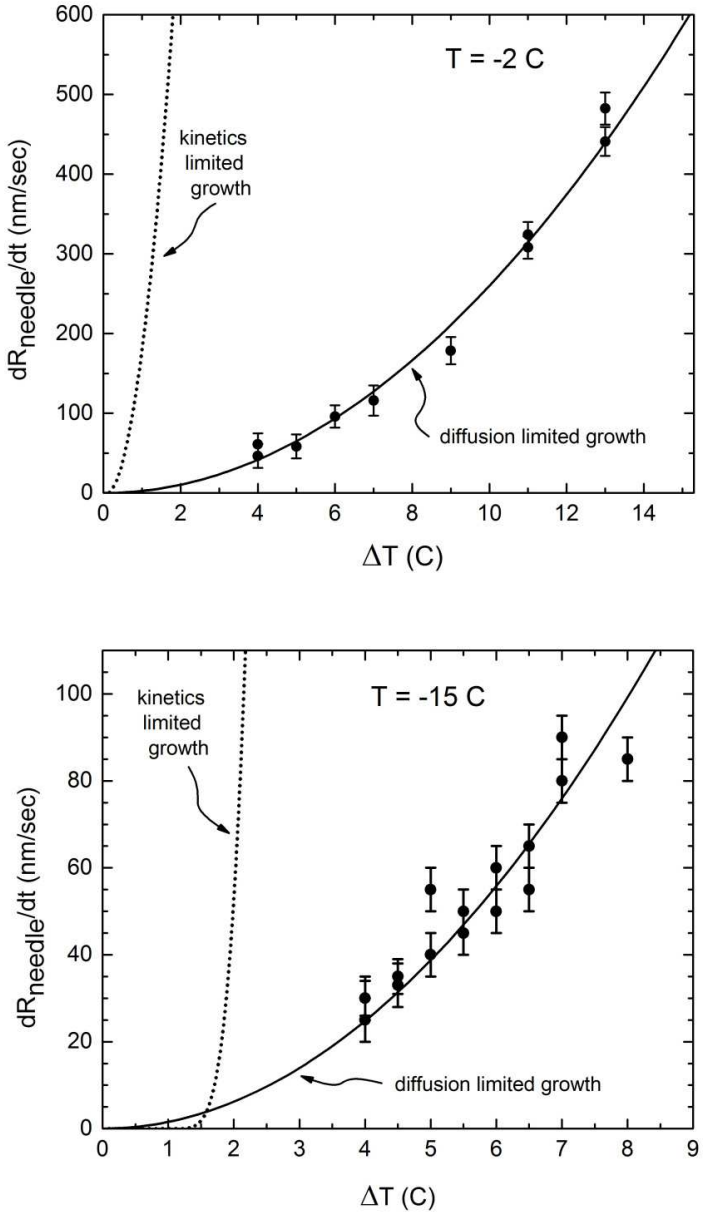

Figure 4: The upper graph shows measurements of $v_5 = dR_{needle}/dt$ when $R_{needle} = 5$ μm, from data taken at a temperature of $T = -2$ C, as described in the text. The lower graph shows similar data taken at $T = -15$ C. Both data sets were fit to quadratic functions $v_5 = A_5 \Delta T^2$, shown as solid lines. This functional form is expected if the growth is predominantly limited by diffusion, and not by attachment kinetics. The dotted lines in both graphs show models of what the velocities would be if the growth were limited instead by attachment kinetics.

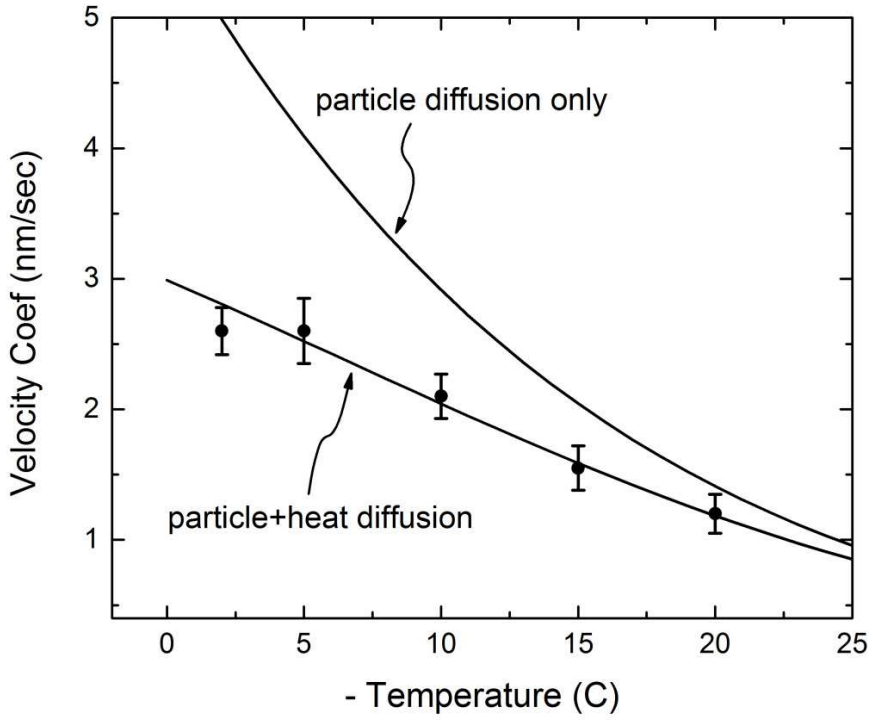

Figure 5: The points show the measured velocity fit coefficient $A_5(T)$ as a function of the crystal growth temperature. For comparison we show calculated $A_5(T)$ for particle diffusion only (upper curve, Equation 8) and for combined particle diffusion and heat diffusion (lower curve, Equation 10). Both curves used $G_{mod} = 0.72$ and $R_{far} = 2$ cm, after adjusting R_{far} so the lower curve best fit the observational data.

References

[1] Kenneth G. Libbrecht. A dual diffusion chamber for observing ice crystal growth on c-axis ice needles. *arXiv:*, (1405.1053), 2014.

[2] U. Nakaya. *Snow Crystals*. Harvard University Press: Cambridge, 1954.

[3] B. J. Mason, G. W. Bryant, and A. P. Van den Heuvel. The growth habits and surface structure of ice crystals. *Phil. Mag.*, 8:505–526, 1972.

[4] D. Lamb and W. D. Scott. Linear growth rates of ice crystals grown from the vapor phase. *J. Cryst. Growth*, 12:21–31, 1972.

[5] T. Kuroda and R. Lacmann. Growth kinetics of ice from the vapour phase and its growth forms. *J. Cryst. Growth*, 56:189–205, 1982.

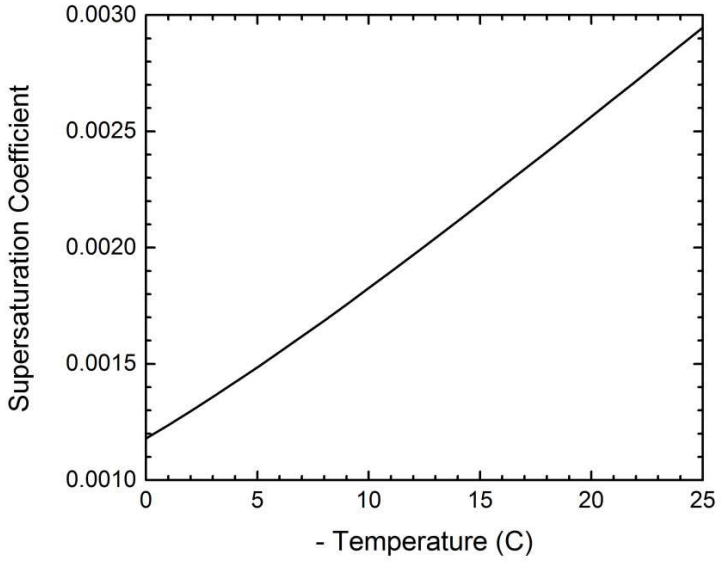

Figure 6: The final supersaturation coefficient $A_\sigma(T)$, giving the effective $\sigma_{far} = A_\sigma(T)\Delta T^2$ for our experimental apparatus. The cylindrical growth data thus calibrate the supersaturation in the growth chamber, corrected for crystal heating, which is valuable for further modeling of more complex growth morphologies.

[6] W. Beckmann, R. Lacmann, and A. Blerfreund. Growth rates and habits of ice crystals grown from the vapor phase. *J. Phys. Chem.*, 87:4142–4146, 1983.

[7] Jon Nelson and Charles Knight. Snow crystal habit changes explained by layer nucleation. *J. Atmos. Sci.*, 55:1452–1465, 1998.

[8] K. G. Libbrecht. The physics of snow crystals. *Rep. Prog. Phys.*, 68:855–895, 2005.

[9] Kenneth G. Libbrecht and Mark E. Rickerby. Measurements of surface attachment kinetics for faceted ice crystal growth. *J. Crystal Growth*, (377):1–8, 2013.